

# PRIMERJALNA ANALIZA METOD PSINSAR, SBAS IN KOMBINIRANE METODE ZA DOLOČITEV POGREZANJA POVRŠJA V MESTU ORAN, ALŽIRIJA

# ASSESSING GROUND DISPLACEMENT IN ORAN CITY, ALGERIA: A COMPARATIVE ANALYSIS OF PSINSAR, SBAS, AND COMBINED METHOD

Kamel Hasni, Bachir Gourine, Boudhane Boubaker, Slimani Mohammed El Amine

UDK: 551.242:543.453(651)

Klasifikacija prispevka po COBISS.SI: 1.01

Prispelo: 21. 5. 2024

Sprejeto: 23. 10. 2024

DOI: 10.15292/geodetski-vestnik.2024.04.432-450

SCIENTIFIC ARTICLE

Received: 21. 5. 2024

Accepted: 23. 10. 2024

## IZVLEČEK

Obalna mesta se spopadajo z deformacijo tal, zato je spremljanje časovnega razvoja posedanja površja tal bistvenega pomena. Napredne interferometrične tehnike, kot sta PSInSAR in SBAS, so pomembne za opazovanje tega pojava, saj omogočajo goste meritve premikov za daljše obdobje. Vendar pa ti algoritmi na nekaterih območjih delujejo bolje kot na drugih, zato se kaže vse večja potreba po izboljšanju kakovosti ocenjevanja premikov z razvojem novih kombiniranih metod. V tej študiji so bili za oceno kakovosti meritev premikanja tal v mestu Oran uporabljeni satelitski posnetki Envisat iz let od 2003 do 2010 ter metodi PSInSAR, SBAS in kombinirana metoda. Naši rezultati kažejo, da imata tehniki PSInSAR in SBAS podobne vrednosti povprečnih hitrosti premikov, ki se gibljejo od  $-2,8$  do  $4,4$  mm/leto in od  $-4,6$  do  $4$  mm/leto. PSInSAR daje dobro porazdelitev sipalcev v urbanih območjih in večjo natančnost premikov, z največjim standardnim odklonom  $1,4$  mm/leto, medtem ko SBAS daje dobre rezultate na podeželskih območjih in ima največji standardni odklon  $3,6$  mm/leto. Rezultat kombinirane metode je bil gostejši in z več zaznanimi sipalci. Povprečna hitrost premikov se je gibala od  $-4,6$  do  $4,2$  mm/leto, z dobro porazdelitvijo na urbanih in ruralnih območjih. Na splošno so bili premiki s kombinirano metodo ocenjeni natančneje kot z drugima tehnikama, kar kaže, da bi lahko postala učinkovito orodje za spremljanje sprememb tal.

## KLJUČNE BESEDE

PSInSAR, SBAS, kombinirana metoda, Oran, pogrezanje površja

## ABSTRACT

Coastal cities are grappling with ground deformation, making monitoring the temporal evolution of ground subsidence crucial. Advanced interferometric techniques, such as PSInSAR and SBAS provide a pertinent mean to observe this phenomenon by supplying dense displacement measurements for an extended period. However, while these algorithms have proven their effectiveness in some areas, their performance is less consistent in others. As such, there is a growing need to enhance the quality of displacement estimation through the development of new combination methods. In this study, Envisat images were used to assess the measurement quality of the displacement over Oran city using PSInSAR, SBAS, and a fusion technique from 2003 to 2010. Our findings indicate that PSInSAR and SBAS techniques mean velocities have similar values, ranging from  $-2.8$  to  $4.4$  mm/yr and  $-4.6$  to  $4$  mm/yr, respectively. Though, PSInSAR demonstrated a good distribution in urban areas and a greater precision, with a maximum standard deviation of  $1.4$  mm/yr, compared to SBAS that performed well in rural areas and which had a maximum standard deviation of  $3.6$  mm/yr. The combination method outcome was denser with a higher number of detectable pixels. Its mean velocity ranged from  $-4.6$  to  $4.2$  mm/yr, with a better distribution in both urban and rural areas. Overall, the combination technique estimated displacements with better precision than the other methods, highlighting its potential as an effective tool for monitoring ground deformation.

## KEY WORDS

PSInSAR, SBAS, combined method, Oran, subsidence

## 1 INTRODUCTION

Interferometric Synthetic Aperture Radar (InSAR) (Zebker and Villasenor, 1992) offers a versatile and efficient approach to monitoring land subsidence (Amighpey and Arabi, 2016). Its ability to capture data independently of weather conditions, coupled with its extensive spatial coverage and high resolution, makes it a valuable tool for investigating historical and ongoing subsidence patterns. A wide range of factors, including human activities such as groundwater extraction and mining, as well as natural processes like volcanic activity and earthquakes, can induce land subsidence, which InSAR excels at detecting and quantifying (Massonnet and Fiegl, 1998). While InSAR provides a powerful means of analysis, its data can be influenced by various error sources. To address some of these challenges and enhance measurement precision, advanced techniques like Persistent Scatterer InSAR (PSInSAR) (Ferretti et al., 2001; Hooper et al., 2004) and Small Baseline Subset (SBAS) (Berardino et al., 2002; Hooper, 2008) have been developed. They are now widely used for monitoring ground displacements.

The PSInSAR method relies on a collection of Synthetic Aperture Radar (SAR) images acquired over the same area. From this dataset, a single reference image is selected, carefully considering factors like acquisition time and satellite position to ensure the identification and tracking of stable ground features with reliable radar backscatter known as Persistent Scatterers (PS) across all image pairs (Ferretti et al., 2001; Hooper et al., 2004). In urban environments, buildings and underlying surfaces often provide stable points for measurement (Colesanti et al., 2003; Perissin et al., 2012), leading to high PS-InSAR reliability and accuracy. However, in rural or less developed areas, the scarcity of such stable points can compromise the technique's precision. SBAS, on the other hand, is a technology used to monitor surface displacements in areas with complicated deformation patterns (Berardino et al., 2002), such as seismically active zones (Qiu et al., 2019) or places with uneven ground movement (Zhao et al., 2019). It is a multi-temporal InSAR technique that analyses phase information from numerous pairs of SAR images acquired in a short period of time (Hu et al., 2018). SBAS focuses on monitoring localized deformations and provides a dense network of displacement measurements by selecting subsets of image pairings with small perpendicular baselines. This methodology is particularly effective for rapid or localized ground movements such as landslides (Liu et al., 2019), subsidence (Amighpey et al., 2016), or volcanic activity (Solaro et al., 2010).

While PSInSAR and SBAS techniques offer distinct advantages, their complementary nature, particularly in diverse environments, has been recognized. However, the efficacy of both methods can be compromised in regions characterized by dynamic land cover, rapid urbanization (Zhang et al., 2023; Yan et al., 2018), or complex deformation patterns (Hooper et al., 2012). To address these limitations, fusion approaches such as SqueeSAR (Ferretti et al., 2011) and StaMPS/MTI (Hooper, 2008) have emerged. These techniques combine the strengths of PSInSAR and other scattering models to produce more accurate and spatially comprehensive deformation maps. By integrating these methodologies, it is possible to generate reliable displacement measurements, even in challenging conditions.

Oran is the second biggest city in Algeria. It is vulnerable to landslides due to its rugged environment and geological characteristics. The surrounding mountains have steep slopes and unstable rock formations, increasing the potential of landslides, particularly during seasons of severe rainfall (Mammar et al., 2016). In terms of earthquakes, Oran is situated in a seismically active zone caused by the convergence of

the African and Eurasian tectonic plates (Bouhadad et Laouami, 2002; Allal et al., 2023). Several strong earthquakes have occurred in the area in the past, indicating the presence of potential seismic danger. Earthquakes, by weakening soils and rock formations, can cause severe damage to urban structures and increase the risk of landslides. As a result, it is critical to consider the seismic danger in Oran's urban design and risk management, by establishing suitable prevention and preparedness measures to reduce the possible effects of earthquakes on the people and city infrastructure.

This study employs a comparative analysis of three Multi-Temporal InSAR (MT-InSAR) techniques - PSInSAR, SBAS, and a combined method - to quantify ground displacement within the city of Oran utilizing Envisat satellite data. By generating mean velocity maps for each method, this research aims to evaluate their relative performance and assess the potential benefits of a combined method.

## 2 METHODOLOGY

### 2.1 PSInSAR processing

During the SAR processing, the phase of each pixel is calculated by coherently combining the contributions of all targets within its resolution cell. However, spatio-temporal decorrelation can cause unstable phase measurements in the interferometric processing, potentially compromising the accuracy. Fortunately, a special group of pixels remains resilient to this phenomenon those containing a strong, dominant scatterer within their resolution cell. This dominant target's contribution overpowers others, ensuring a stable phase measurement over time (Ferretti et al., 2001). The PSInSAR takes advantage of these resilient pixels, known as PS, which serve as reliable anchors, enabling to achieve a remarkable precision in mapping ground deformation rates and temporal evolution down to the millimetre scale (Ferretti et al., 2001; Hooper et al., 2004). A variety of software packages are available for PSInSAR processing, including SARPROZ (Perissin et al., 2012), SARscape (Agarwal et al., 2020), and STaMPS/MTI (Hooper et al., 2004). In the following, the methodology describes STaMPS/MTI procedure for PSInSAR used in this study. A detailed description of the algorithm is presented in Figure 1.

The initial step of PSInSAR processing entails the creation of  $N$  interferograms from a dataset of  $N+1$  images, with one image designated as a reference (Hooper et al., 2004). Subsequent removal of the topographic phase component, achieved through the application of a Digital Elevation Model (DEM), isolates a signal influenced by five primary factors:

$$\Phi_{x,i} = \Phi_{disp,x,i} + \Phi_{atmo,x,i} + \Phi_{orb,x,i} + \Phi_{\epsilon,x,i} + n_{x,i} \quad (1)$$

Where:

- $\Phi_{disp,x,i}$  represents the phase of the  $i^{\text{th}}$  interferogram related to surface movement of the pixel ( $x$ ) in the Line Of Sight (LOS) direction.
- $\Phi_{atmo,x,i}$  accounts for the slight delay induced in the signal by the atmosphere, which varies between satellite passes and impacts measurement accuracy.
- $\Phi_{orb,x,i}$  is related to the imperfections in the satellite's path that can also introduce inaccuracies in the final measurement.

- $\Phi_{\epsilon,x,i}$  is the influence that might remain due to any errors present in the DEM itself.
- $n_{x,i}$  encompasses various sources of variability, including how the signal scatters from the observed area, instrument noise, and errors during images coregistration. A pixel is called PS if the noise level  $n_{x,i}$  is low enough to not completely hide the important information.

To identify PS candidates, we employed a metric known as “amplitude dispersion” ( $D_A = \sigma_A/\mu_A$ ). It is computed by determining the ratio of a pixel’s standard deviation ( $\sigma_A$ ) to its mean value ( $\mu_A$ ). While effective for high signal-to-noise ratio (SNR) targets where amplitude dispersion is strongly correlated with phase stability, the reliability of this approach diminishes for objects with lower SNR due to a breakdown in this relationship (Hooper et al., 2004).

The StaMPS/MTI algorithm posits that deformation, atmospheric, and orbital components exhibit spatial correlation within a specified distance ( $L$ ), while topography and noise do not. By calculating the mean phase of neighbouring pixels within a circular patch with radius ( $L$ ) centred at the pixel ( $x$ ) we get:

$$\bar{\Phi}_{x,i} = \bar{\Phi}_{disp,x,i} + \bar{\Phi}_{atmo,x,i} + \bar{\Phi}_{orb,x,i} + \bar{n}_{x,i} \tag{2}$$

Here the bar accounts for the patch mean and  $\bar{n}_{x,i}$  is the sum of the means of  $\Phi_{x,i}$  and  $n_{x,i}$  is assumed to be small. Subtracting equation (2) from equation (1) leads to:

$$\Phi_{x,i} - \bar{\Phi}_{x,i} = \Phi_{\epsilon,x,i} + n_{x,i} - \bar{n}_{x,i} \tag{3}$$

Where:  $\bar{n}_{x,i} = \bar{n}_{x,i} + (\bar{\Phi}_{disp,x,i} - \Phi_{disp,x,i}) + (\bar{\Phi}_{atmo,x,i} - \Phi_{atmo,x,i}) + (\bar{\Phi}_{orb,x,i} - \Phi_{orb,x,i})$ .

For a number of  $N$  interferograms, a phase stability metric  $\gamma_x = (1/N) \sum_{i=1}^N \exp\{j(\Phi_{x,i} - \bar{\Phi}_{x,i} - \hat{\Phi}_{\epsilon,x,i})\}$  is defined based on the temporal coherence. Where  $\hat{\Phi}_{\epsilon,x,i}$  is the estimate of  $\Phi_{\epsilon,x,i}$ , which is determined by Least-squares from equation (3), since it is the only quantity correlated with the perpendicular baseline (Hooper et al., 2004). The PS candidates are initially selected based on high amplitude dispersion threshold (usually  $D_A \leq 0.4$ ). Followed by an iterative approach employed to calculate a preliminary value of  $\gamma_x$ , pixels exhibiting higher  $\gamma_x$  are more likely to be classified as PS. In the next step, we temporarily eliminate candidates having low  $\gamma_x$  scores and recompute patch means using only the qualified candidates. The value of  $\gamma_x$  is calculated again for all the pixels. This iterative approach serves to minimize  $\bar{n}_{x,i}$ . After enough number of iterations, the quantity  $\bar{n}_{x,i}$  is reduced and  $\gamma_x$  is now dominated by  $n_{x,i}$  (equation 3).

The final step in the selection of PS resides in the definition of a threshold  $\gamma^*$  for the temporal correlation that maximizes the number of real PS and minimizes the number of false PS bellow a value ( $q$ ). The search for this value is done statically by the delimitation of the Probability Density Function (PDF) of  $\gamma_x$  defined as:

$$p(\gamma_x) = (1 - \alpha)p_r(\gamma_x) + \alpha p_{ps}(\gamma_x) \tag{4}$$

Where:  $p_r$  accounts for the random phase pixels (false PS), and  $p_{ps}$  stands for the non-random phase pixels (real PS). The threshold  $\gamma^*$  should verify:

$$(1 - \alpha) \int_{\gamma^*}^1 p_r(\gamma_x) d\gamma_x / \int_{\gamma^*}^1 p(\gamma_x) d\gamma_x = q \tag{5}$$

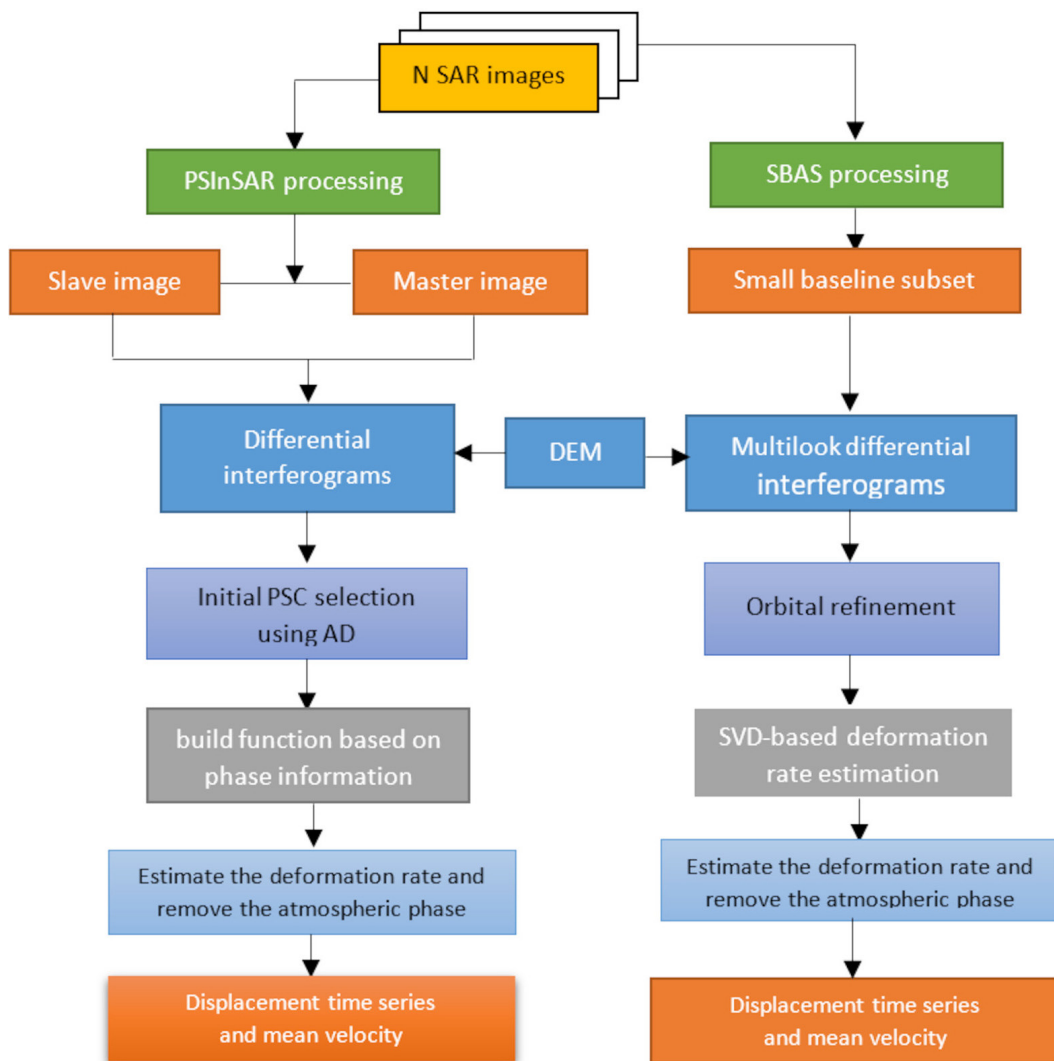


Figure 1: Flowchart of PSInSAR and SBAS processings implemented in StaMPS/MTI

## 2.2 SBAS processing

The Small BAseline Subset (SBAS) method is an effective approach designed to produce time-series data on surface deformation by examining extensive sequences of SAR images captured over the same geographic area. This technique effectively tackles the complexities associated with accurately monitoring ground movements, including subsidence and uplift. SBAS utilizes pairs of SAR images obtained from slightly different orbital positions at different acquisition times. The interferometric phase difference observed in these pairs provide critical insights into terrain deformation. A significant challenge in this process is distinguishing the deformation signal from other phase contributions, such as variations in terrain height (Hooper, 2008).

Considering a set of  $(N+1)$  SAR images acquired at ordered times  $t_0, t_1, t_2, \dots, t_N$ . Each acquisition can interfere with at least one other image to form small baseline differential interferograms. If there are  $(M)$  differential interferograms, the following inequality is satisfied (Berardino et al., 2002):

$$\frac{N+1}{2} \leq M \leq N \left( \frac{N+1}{2} \right) \tag{6}$$

A  $j$ -interferogram expressed in radar azimuth and range coordinates  $(x, r)$ , generated from the dates  $t_B$ , and  $t_A$ , can be expressed as:

$$\begin{aligned} \delta\Phi_j(x, r) = \Phi(t_B, x, r) - \Phi(t_A, x, r) \approx & \frac{4\pi}{\lambda} [d(t_B, x, r) - d(t_A, x, r)] + \frac{4\pi}{\lambda} \frac{B_{\perp j} \Delta z}{r \sin \theta} \\ & + [\Phi_{atm}(t_B, x, r) - \Phi_{atm}(t_A, x, r)] + \Delta n_j \quad \forall j = 1, \dots, M \end{aligned} \tag{7}$$

The right part of equation (7) considers four components:

- The first term  $d(t_B, x, r)$  and  $d(t_A, x, r)$  accounts for the cumulative LOS displacement at times  $t_B$  and  $t_A$  respectively, taking  $t_0$  as the reference for the displacements (assuming the phases are unwrapped). Where  $\lambda$  is the system wavelength.
- The second term, represented by  $\frac{4\pi}{\lambda} \frac{B_{\perp j} \Delta z}{r \sin \theta}$ , accounts for potential phase errors (artifacts) that may arise during the interferometric phase generation process due to inaccuracies in the assumed topography of the scene. The influence of these errors depends on the separation between the satellite orbits. Here  $B_{\perp j}$  accounts for the perpendicular baseline,  $\Delta z$  is the altitude of the pixel,  $r$  is the range distance (sensor-target distance) and  $\theta$  stands for the look angle.
- The third term denoted by  $\Phi_{atm}(t_B, x, r) - \Phi_{atm}(t_A, x, r)$ , accounts for potential phase errors caused by variations in atmospheric properties between the acquisitions at times  $t_A$  and  $t_B$ . This term is often called the Atmospheric Phase Screen (APS).
- Finally, the term  $\Delta n_j$  incorporates phase contributions arising from the baseline, temporal decorrelation, and thermal noise effects.

In the SBAS technique, the selected pixels for which the deformation is to estimate are called Slowly-Decorrelating Filtered Phase (SDFP) pixels. These pixels exhibit minimal phase variation over short temporal intervals. By analysing their amplitude, a subset of pixels most likely containing SDFP points can be efficiently identified. This stability is quantified by the Amplitude Difference Dispersion (ADD) index, computed as the standard deviation of amplitude differences between master and slave images divided by the mean amplitude. ADD is analogous to the established amplitude dispersion (AD) index used for point scatterers but offers enhanced accuracy when spectral filtering is applied (Hooper, 2008). We used a threshold of  $(D_{\Delta A} \leq 0.6)$  in our work.

The system for the unwrapped interferometric phase  $\delta\Phi$  is expressed as:

$$\delta\Phi = BGP \tag{8}$$

Where  $\delta\Phi$  is the  $M \times 1$  vector of measured interferograms,  $B$  is a  $M \times N$  matrix defined as  $B(j, k) = t_{k+1} - t_k$  for  $I_{S_j} + 1 \leq k \leq I_{E_j}, \forall j = 1, \dots, M$  and  $B(j, k) = 0$  elsewhere, taking into account the assumption that the master (IE) and the slave (IS) are chronologically ordered  $(I_{E_j} > I_{S_j}, \forall j = 1, \dots, M)$ .  $G$  is a  $M \times L$

matrix where the columns characterize vector components of the velocity, and  $P$  is the  $L \times 1$  deformation model vector of unknown cumulative deformation phases between acquisition times. In case of a consideration of a cubic deformation model, the phase variation is defined as:

$$\Phi(t_i) = \bar{v}(t_i - t_0) + \frac{1}{2}\bar{a}(t_i - t_0)^2 + \frac{1}{6}\Delta\bar{a}(t_i - t_0)^3 \quad (9)$$

Here  $\bar{v}$ ,  $\bar{a}$  and  $\Delta\bar{a}$  are the mean velocity, acceleration and acceleration variation unknown parameters respectively. The vector  $P$  is defined in this case as  $P^T = [\bar{v}, \bar{a}, \Delta\bar{a}]$ . Due to the sparsity of the matrix  $B$ , it becomes rank deficient. This makes the system underdetermined with an infinite number of solutions. To solve this system, we use the Singular Value Decomposition (SVD) method (Berardino et al., 2002).

### 2.3 Combination of PSInSAR and SBAS

The combined PSInSAR and SBAS method is a powerful tool for improving the accuracy and spatial resolution of surface displacement measurements, by utilizing the results of both algorithms. This approach combines the strengths of PSInSAR in urban areas and SBAS in rural or natural areas. Additionally, the spatial resolution of measurements is enhanced by using data from both methods (Hooper, 2008; Hooper et al., 2013). The combined method selects the most favourable pixels from the PSInSAR and SBAS results to improve the spatial sampling of the signal, resulting in more accurate and reliable measurements of surface displacements.

We consider StaMPS/MTI algorithm (Hooper, 2008) to combine PSInSAR and SBAS techniques (Figure 2). This combined approach increases the amount of usable signal data collected over a wider area, ultimately leading to more accurate results in Multi-Temporal analysis. Better spatial sampling does not only improve the resolution of deformation signal but it also aids in the reliable estimation of phase ambiguities, which is crucial for the accurate unwrapping of phase data and the subsequent derivation of deformation fields. To estimate the spatially correlated contribution of neighbouring pixels, a bandpass filter is utilized. Additionally, an estimate of the coherence magnitude is provided by (Hooper et al., 2007):

$$\gamma_x = \frac{1}{N} \left| \sum_{i=1}^N \exp \left\{ \sqrt{-1} \left( \psi_{x,i} - \tilde{\psi}_{x,i} - \Delta\hat{\Phi}_{\theta,x,i}^u \right) \right\} \right| \quad (10)$$

In this equation,  $\psi_{x,i}$  corresponds to the wrapped phase pixel in the interferogram ( $i$ ), while  $\tilde{\psi}_{x,i}$  represents the spatially correlated pixels.  $\hat{\Phi}_{\theta,x,i}^u$  is descriptive of pixels that are not spatially correlated. Finally, ( $N$ ) represents the number of generated interferograms.

The combination between PSInSAR-SBAS enables the calculation of the equivalence between SBAS and PSInSAR interferograms. When a pixel has both PS and SDFP values, the algorithm assigns the average values of the phase obtained from the results of the PSInSAR and SBAS processing to the pixel. This approach combines information from both methods to enhance the accuracy and reliability of the measurement and the total number of scatterers obtained from PSInSAR and SBAS processing. The combination enhances the SNR defined by  $SNR = 1/(\gamma_x^{-1} - 1)$  (Hooper, 2008). This method is considered more robust and efficient for measuring surface deformations.

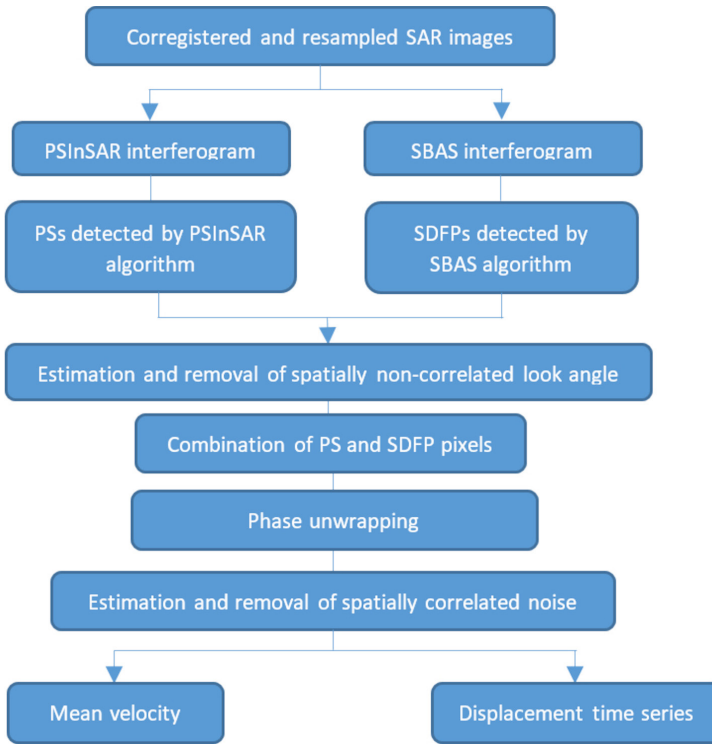


Figure 2: Flowchart of the combined method between PSInSAR and SBAS methods.

### 3 STUDY AREA

Oran is a coastal city located in the north-west of Algeria; on the Mediterranean coast (Figure 3). It is a dynamic and cosmopolitan port city, with a rich history and diverse culture. The city of Oran is an important economic, commercial, and tourist centre in the region and it is often considered as one of the most attractive cities in the country. The Oran region is characterized by a rugged and ravine fringe followed by a plateau that reaches a peak of around 110 meters. Its geological, tectonic, hydrological, hydrogeological, and meteorological features create a complex physical system where the risk of natural disasters is omnipresent (Bouhadad et Laouami, 2002).

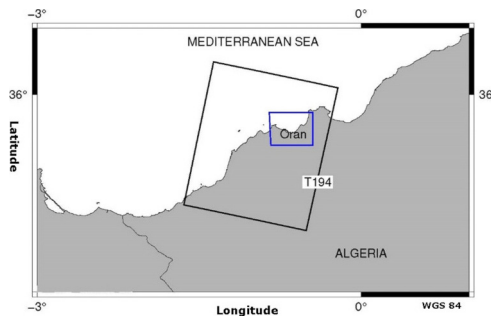


Figure 3: Envisat ASAR satellite track 194 covering Oran region (black rectangle). The blue square represents the study area.

This city presents a variety of geographic, social, and urban characteristics (Mammar et al., 2016). Geographically, the area includes the waterfront with its beaches, adjacent urban neighbourhoods, as well as peripheral areas with natural elements such as hills, rivers, and wetlands. Due to its character, nature, and geographical location, Oran is a city at major risk and potential due to its position in the collision zone between the African and Eurasian tectonic plates, which results in the implications of neotectonics (Alvares-Marron, 1999).

#### 4 DATA USED

In this study, we analysed a dataset consisting of 28 radar images obtained from the European Envisat satellite's ascending track (Track 194) over a period of 7 years, from 04/07/2003 to 27/09/2010 (Table 1). The interferometric processing of these radar images was performed using the DORIS (Delft Object-oriented Radar Interferometric Software) software (DORIS software website). The super master image used in this study was acquired on 27/03/2006. The dataset covers an area of approximately 100x100 km<sup>2</sup>, as illustrated in Figure 3.

Table 1: Envisat data used in this study

ID	Acquisition date	Perpendicular baseline $B_{\perp}$	Temporal baseline (days)
01	2003-04-07	-336.5	-1085
02	2003-05-28	-292	-945
03	2003-12-08	-666.3	-840
04	2004-01-12	103.5	-805
05	2004-02-16	748.5	-770
06	2004-04-26	336.6	-700
07	2004-05-31	240.1	-665
08	2004-10-18	420.1	-525
09	2004-12-27	-159.2	-455
10	2005-01-31	-392	-420
11	2005-04-11	-216	-354
12	2005-05-16	66.9	-315
13	2005-07-25	232.8	-245
14	2005-08-29	376.4	-210
15	2005-11-07	426.4	-140
16	2006-02-20	-488.7	-35
17	<b>2006-03-27</b>	<b>0</b>	<b>0</b>
18	2006-06-05	-841.9	70
19	2006-07-10	672.6	105
20	2007-01-01	116.1	280
21	2007-02-05	-466.4	315
22	2008-05-05	-301.8	770
23	2009-09-07	49	1260
24	2010-01-25	-54.5	1400
25	2010-03-01	-462	1435
26	2010-05-10	-83.2	1505
27	2010-07-19	416.9	1575
28	2010-09-27	32.2	1645

## 5 RESULTS AND DISCUSSION

### 5.1 Results of PSInSAR, SBAS and the combination

This research aims at assessing the displacement of the city of Oran, the two techniques PSInSAR and SBAS were employed on a set of 28 Envisat Single Look Complex (SLC) images spanning the period from 2003 to 2010. The PS (PSInSAR) and SDFP (SBAS) pixels were identified using amplitude dispersion  $D_A \leq 0.4$  and amplitude difference dispersion  $D_{\Delta A} \leq 0.6$  thresholds, respectively. Additionally, we ensured a maximum phase noise standard deviation of 1 rad to guarantee the accuracy of the outcomes (DORIS software website). The multi-temporal processing resulted in a total of 39,215 PS pixels and 47,398 SDFP pixels.

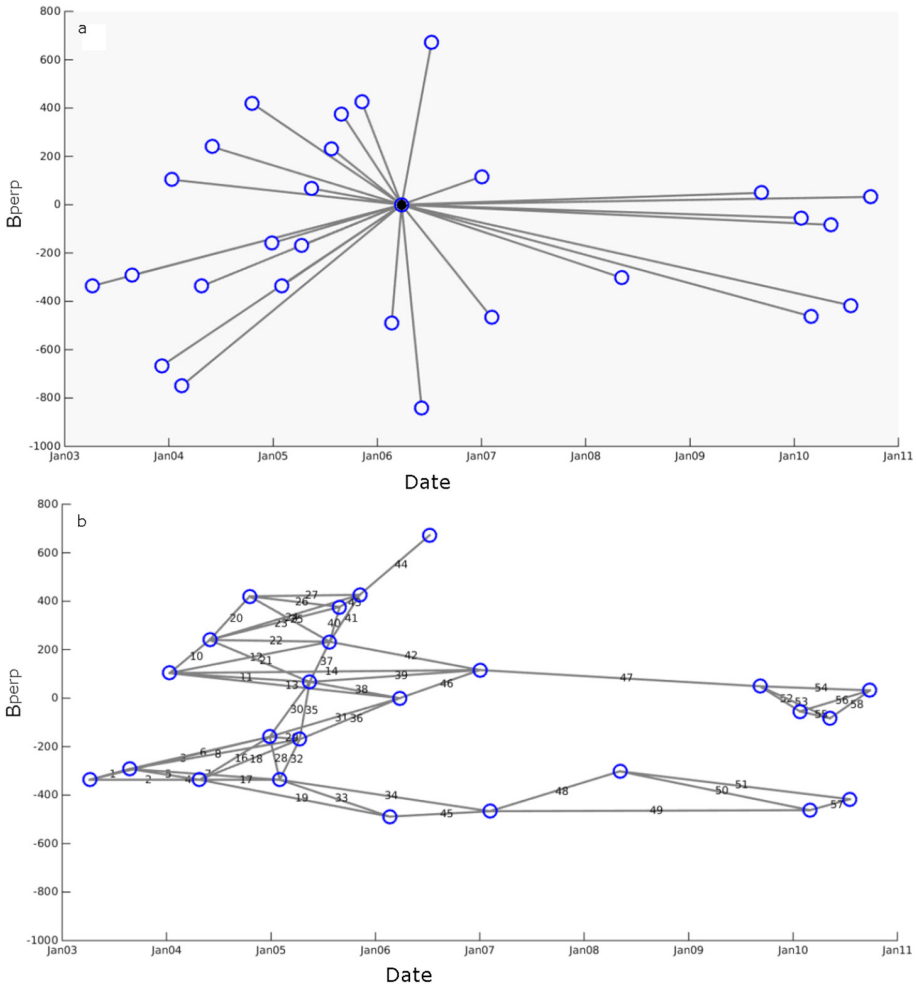


Figure 4: Connection graphs for PSInSAR and SBAS. a) Configuration of spatial and temporal distribution PSInSAR couples, the black point represents the PSInSAR reference image, the blue circles represent the slave images, and the lines stands for the connections between each interferometric pair. b) SBAS connectivity graph, each point represents a SAR image, and lines illustrate the generated interferograms

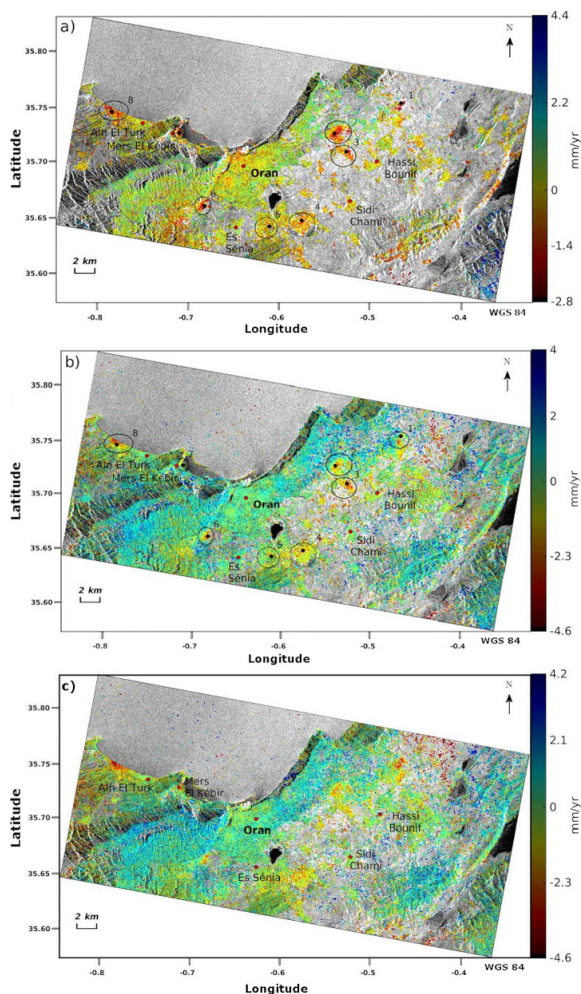


Figure 5: Geocoded mean annual velocities in mm/yr generated from the three methods superimposed over an amplitude image. a) PSInSAR, b) SBAS and c) combined method.

The connection graphs representing the interferometric couples used for PSInSAR and SBAS are presented in Figure 4. Spatial distribution of the selected pixels over Oran region is shown in Figure 5 along with the mean annual LOS displacement velocity for the study period spanning from 2003 to 2010, obtained through PSInSAR, SBAS and the combined method, respectively. A positive LOS velocity denotes ground movement towards the satellite along the LOS, whereas a negative LOS velocity indicates subsidence or movement away from the satellite. The mean annual velocities range from  $-2.8$  to  $4.4$  mm/yr,  $-4.6$  to  $4$  mm/yr and  $-4.6$  to  $2.1$  mm/yr for PSInSAR, SBAS and the combination respectively.

To facilitate a comparative analysis of the derived displacement results from both PSInSAR and SBAS methods, a subset of pixels was selected for in-depth examination. The displacement time series for these chosen pixels are graphically illustrated in Figure 6. The corresponding mean LOS velocity for each pixel is presented in Table 2, as well as the difference between the two velocities.

Table 2: Comparison of PSInSAR and SBAS velocities for some selected pixels.

Pixel	PSInSAR (mm/yr)	SBAS (mm/yr)	difference
P1	-1.7	-1.7	0
P2	-2.8	-2.8	0
P3	-2.4	-2.1	-0.3
P4	-1.3	-1.2	-0.1
P5	-1.7	-1.5	-0.2
P6	-1.8	-1.4	-0.4
P7	-1.8	-2.1	0.3
P8	-2.7	-3.4	0.7

The data presented in Table 2 reveals that the mean annual velocity values for the corresponding pixels from both methods display the same sign, indicating a consistent directional trend, with a minor difference of -0.3 mm/yr and a maximum of 0.7 mm/yr in mean LOS velocity. To provide a more detailed comparative analysis, Figure 6 presents the displacement time series for the initial four pixels highlighted in Figure 5.

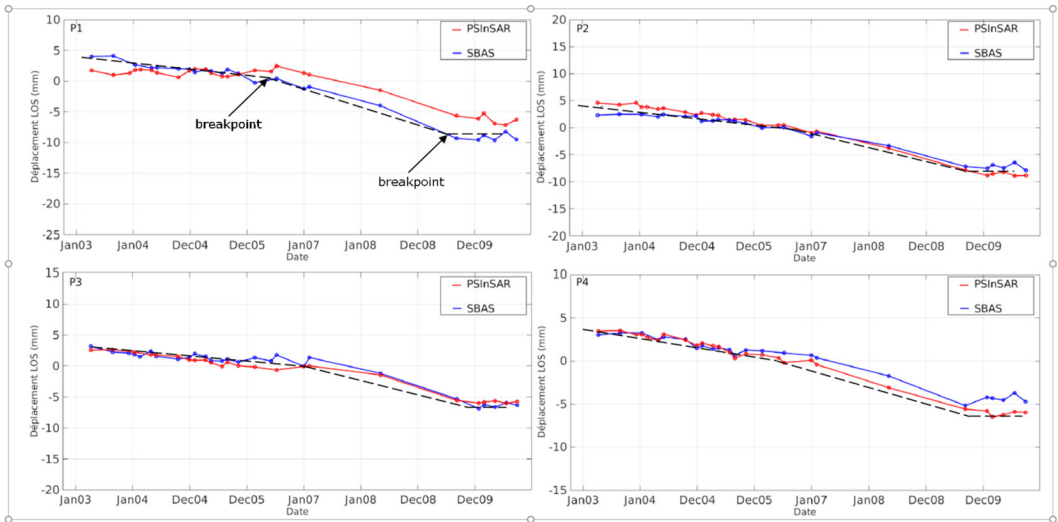


Figure 6: Comparison between displacement time series for the points 1 to 4 located in Figure 5 derived from PSInSAR and SBAS/ Red for PSInSAR and blue for SBAS. The dashed black line is the piecewise linear regression

A comparative analysis of PSInSAR and SBAS-derived displacement time series for four points (Figure 5) reveals distinct deformation patterns. The time series exhibit a general congruence in amplitude and trend, amenable to piecewise linear modelling (Berti et al., 2013), represented by black dashed lines in Figure 6. Three primary deformation phases are discernible:

1. A relatively stable period (2003-2007): Minimal cumulative subsidence ( is observed for points 2, 3 and 4, with exception of point 1 (SBAS: 5 mm).
2. Accelerated subsidence (2007-2009): Significant subsidence rates exceeding 8 mm is evident across all points.
3. Stabilization (2009-2010): Displacement rates diminish to approximately 1 mm.

The phase of PS pixels selected by the PSInSAR technique is combined with the phase of pixels selected by the SBAS technique using the combination algorithm (Hooper, 2008) as described in section 2.3. The mean annual velocity estimated by the combined method is illustrated in Figure 5. The combined method produced an estimated mean velocity range of  $-4.6$  mm/yr to  $4.2$  mm/yr. This method also provided a better spatial coverage of the study area than PSInSAR and SBAS alone, as it selects a greater number of pixels. Specifically, the combined method had 16,000 pixels in common with both techniques.

The analysis of Envisat data using the combined PSInSAR-SBAS approach unveiled a consistent subsidence pattern within Oran region, as depicted in Figure 7. While the combined method replicated the velocity trends observed in both PSInSAR and SBAS results, it demonstrated a significant reduction in data noise.

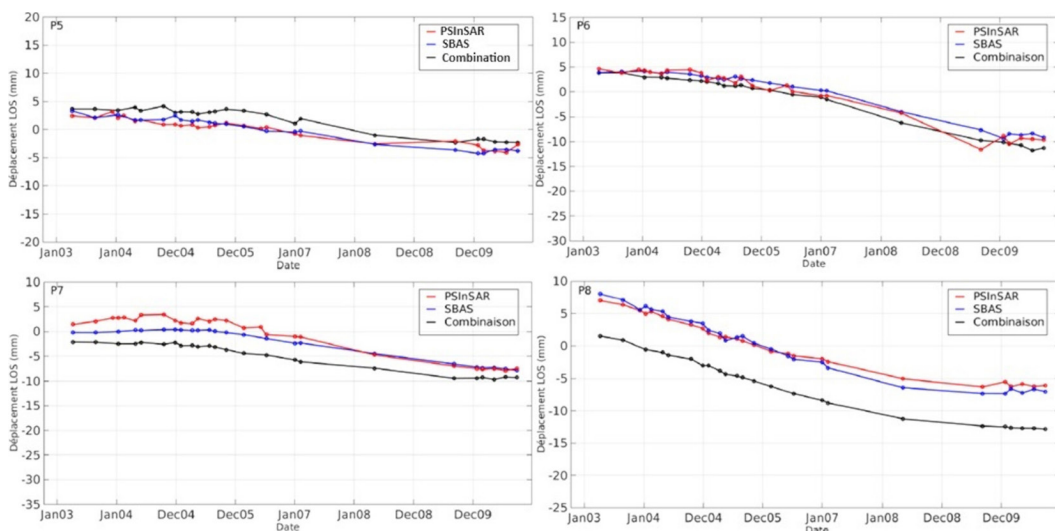


Figure 7: Comparison between displacement time series for the points 1 to 4 located in Figure 5 derived from PSInSAR, SBAS and the combined method. Red for PSInSAR, blue for SBAS and black for the combination

## 5.2 Precision assessment

Accurate quantification of the displacement is paramount for evaluating the reliability and applicability of PSInSAR and SBAS techniques. Given the absence of ground-based measurements in Oran during the study period, which could serve for validation and comparison with alternative methods, an inter-technique comparison was conducted to validate the results. Histograms in Figure 8 indicate that the estimated displacements follow a Gaussian distribution. Furthermore, the calculated standard deviations of the mean velocity are  $0.8$  mm/yr and  $1.2$  mm/yr for PSInSAR and SBAS, respectively. These values suggest relative stability in the region, with approximately 68% of the pixels experiencing displacements within one standard deviation ( $1\sigma$ ). Nevertheless, SBAS demonstrated a higher sensitivity to SDFPs than PSInSAR, resulting in more pixels exhibiting displacement values exceeding  $1\sigma$ .

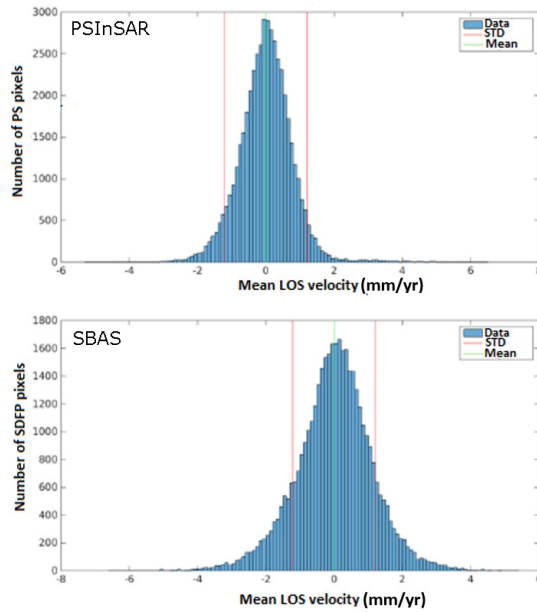


Figure 8: Histograms of mean velocities from PSInSAR and SBAS techniques. The green line shows the mean and the red line accounts for the standard deviation

The measurement precision for a pair of SAR images can be expressed as  $(\lambda/4\pi)\sigma_\phi$  (Eineder and Holzner, 1999), where  $\sigma_\phi$  denotes the standard deviation of phase noise in the interferogram. When  $N$  interferograms are employed, the mean annual velocity can be estimated with an accuracy of  $(4/\sqrt{N})(\lambda/4\pi)\sigma_\phi$  (El Rai and Simonetto, 2010). These theoretical calculations provide insights about the precision that can be achieved. Figure 9 illustrates the precision maps of the mean annual LOS velocities obtained from three techniques.

Figure 9 demonstrates that PSInSAR exhibits superior mean velocity precision, ranging from 0.2 to 1.4 mm/yr, compared to SBAS, whose values fluctuate between 0.4 and 3.6 mm/yr. This disparity can be attributed to the predominant urban location of PSInSAR-detected pixels, where spatiotemporal decorrelation is less pronounced. In contrast, SBAS identifies pixels in both urban and rural areas, leading to increased decorrelation effects and consequently higher standard deviations. Notably, 90% of PSInSAR pixels exhibit a standard deviation below than 0.8 mm/yr, while this threshold is reached for only 50% of SBAS pixels at the 2 mm/yr level.

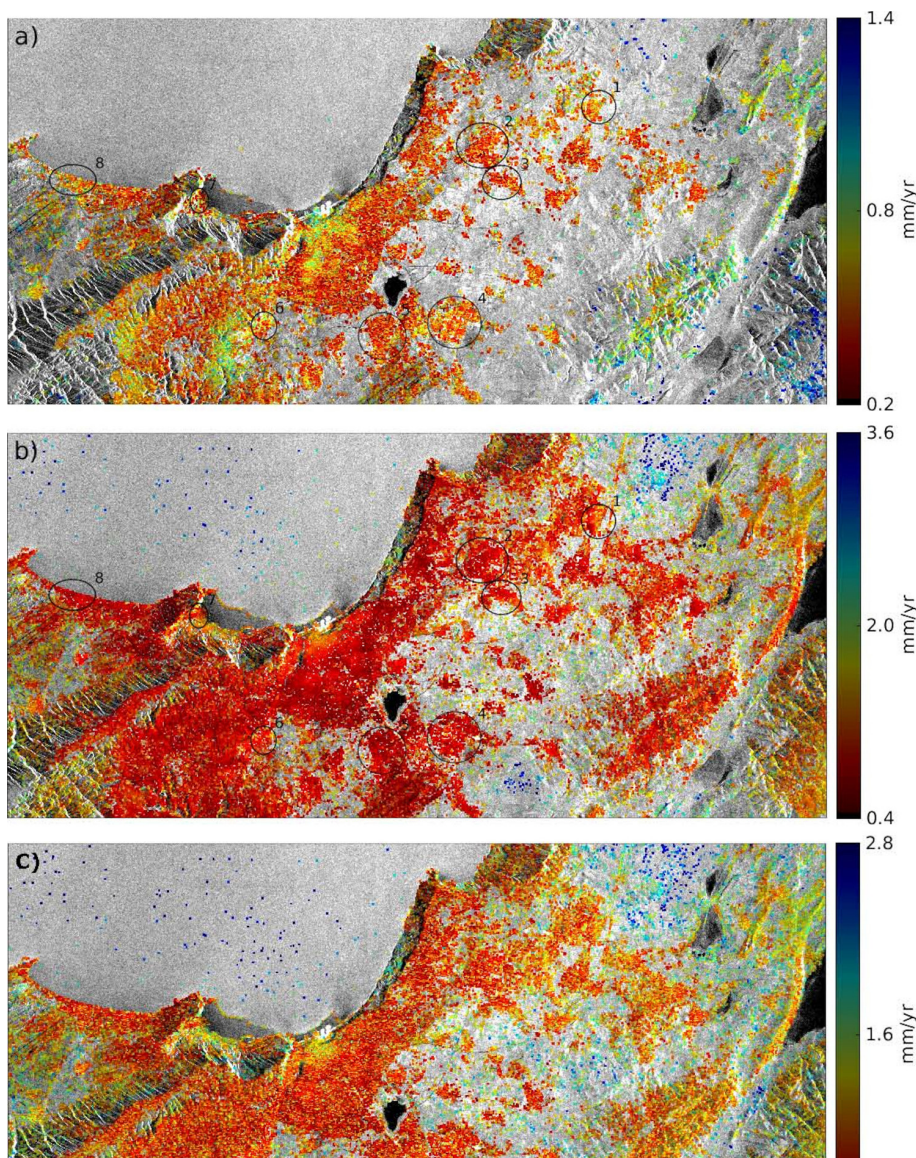


Figure 9: Geocoded precision of the mean annual velocities in mm/yr generated from the three methods superimposed over an amplitude image. (a) PSInSAR, b) SBAS and c) combined method. Low values of standard deviation are coded in red and high values in blue.

To rigorously assess the precision of the velocity estimates, histograms of the standard deviation for both PSInSAR and SBAS-derived mean velocities were plotted (Figure 10). PSInSAR pixels exhibited a mean standard deviation of 0.5 mm/yr with a standard deviation of 0.2 mm/yr, indicating greater precision. In contrast, SBAS-derived pixels displayed a higher mean standard deviation of 1 mm/yr and a standard deviation of 0.4 mm/yr. These findings corroborate the notion that PSInSAR delivers more precise velocity measurements compared to SBAS (Hooper et al., 2012).

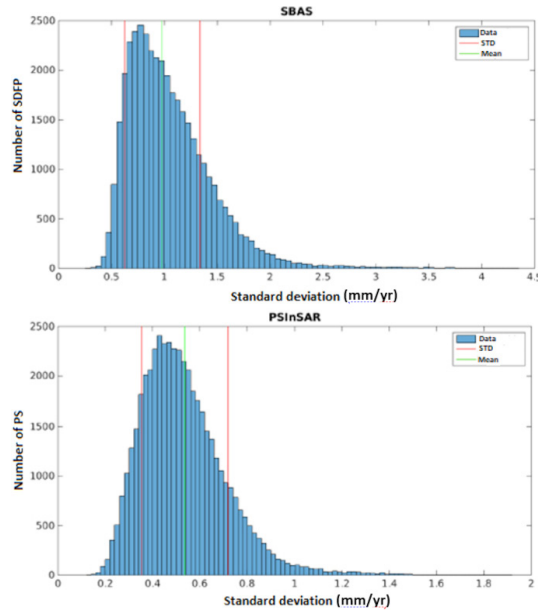


Figure 10: Histograms of standard deviation distribution of mean velocity for PSInSAR and SBAS techniques.

Comparative analysis of histograms in Figure 11 reveals that the combined method outperforms both PSInSAR and SBAS in terms of mean annual velocity precision. The combined method’s standard deviation centre’s around 0.5 mm/yr, significantly lower than the 0.8 mm/yr and 1.2 mm/yr values for PSInSAR and SBAS, respectively. This enhanced precision leads to more reliable ground displacement velocity estimates. Figure 12, the average velocity precision map, corroborates these findings, with the majority of pixels exhibiting sub-0.6 mm/yr precision despite a maximum of 2.8 mm/yr. Time series comparisons in Figure 13 further illustrate the combined method’s effectiveness.

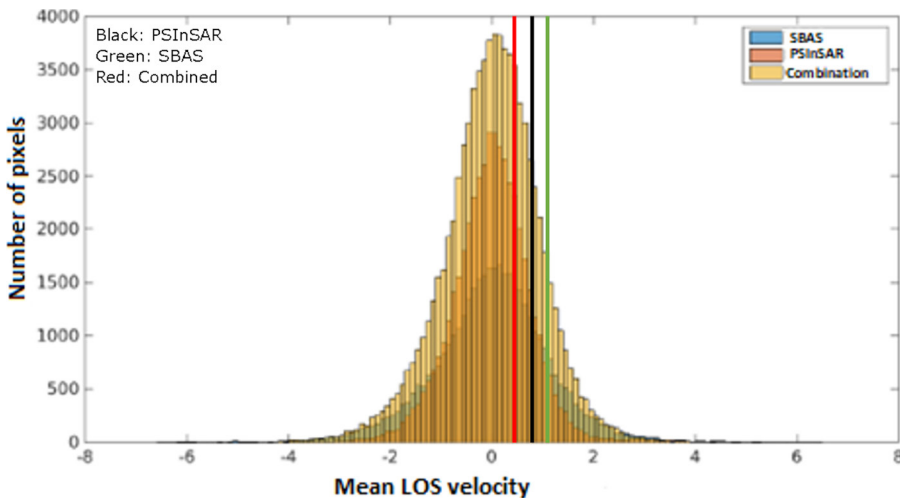


Figure 11: Histogram of mean annual velocities of the PSInSAR, SBAS, and combined methods. The three vertical lines represents the standard deviation of the mean LOS velocity for each method.

The combination of the PSInSAR and SBAS techniques proved to be an effective method for detecting and measuring ground displacement velocities, with better spatial coverage and higher precision compared to using each method separately. The results obtained from our study provide valuable information for monitoring and mitigating potential hazards and risks associated with ground displacements in the area.

## 6 CONCLUSION

In this study, we presented the basic principles of three multi-temporal processing techniques, namely PSInSAR, SBAS, and their combined method. We applied the StaMPS/MTI solution to a series of 28 SLC images covering the Oran region between 2003 and 2010. Our results showed that the city of Oran is relatively stable, but a significant subsidence in some areas surrounding the city was detected. A comparison between the three techniques was conducted to validate the results and demonstrate the potential of the combined method to improve the quality of the results in terms of spatial coverage and signal quality. The comparison showed that both PSInSAR and SBAS techniques detected major displacements in the region. Moreover, the location and magnitude of the displacements measured by the two different techniques have a strong correlation with each other.

The analysis of the velocity precision estimated by PSInSAR and SBAS methods showed that PSInSAR offers better precision with a maximum of 2.8 mm/yr of standard deviation compared to SBAS (3.6 mm/yr). Furthermore, the statistical analysis of the results of the combined method, demonstrated its potential to combine the advantages of the two methods. In conclusion, this study presents a comprehensive analysis of three multi-temporal processing techniques for monitoring ground deformation in the Oran region. Although further validation using ground-based data such as GPS or precision levelling is needed, our results show that the combined method has significant potential for monitoring ground deformation in urban and rural areas.

## References:

- Agarwal., V. Kumar, A., Gomes, R.L., Marsh, S. (2020). An overview of SAR sensors and software and a comparative study of open source (SNAP) and commercial (SARscape) software for DInSAR analysis using C-band radar images. ACR 2020 conference, November 2020, CHINA.
- Allal, S.H., Eladj, S., Dekkiche, H., Hasni, K., Betchime, Y. (2023). Recent Euler pole parameters and relative velocities of the Nubia–Eurasia and Nubia–South America plates estimated using GPS technique. *Acta Geophysica*, 71, 1149–1171. DOI: <https://doi.org/10.1007/s11600-023-01031-6>
- Alvares-Marron, J. (1999). Pliocene to Holocene structure of the eastern Alboran Sea (Western Mediterranean). R. Zahn, M. C. Comas, A. Klaus (Eds), *Proceeding Ocean Drill Program Science Results*, 161, 345–355.
- Amighpey, M., Arabi, S. (2016). Studying land subsidence in Yazd province, Iran, by integration of InSAR and levelling measurements. *Remote Sensing Applications: Society and Environment*, 4, 1–8. DOI: <https://doi.org/10.1016/j.rsase.2016.04.001>.
- Benbakhti, I. M., Maouche, S., Belhaj, D., Harbi, A., Ritz, J-F., Rabai, G., Rezouk, A., Doumaz, F. (2018). Characterizing the active tectonics in the Oran region (Algeria) and recasting the 1790 earthquake. *Journal of Seismology*, 22, 1549–1561. DOI: <https://doi.org/10.1007/s10950-018-9784-3>.
- Berardino, P., Fornaro, G., Lanari, R., Sansosti, E. (2002). A new algorithm for surface deformation monitoring based on small baseline differential SAR interferograms. *IEEE Transactions on Geoscience and Remote Sensing*, 40, 2375 – 2383.
- Berti, M., Corsini, A., Franceschini, S., Iannaccone, M. C. (2013). Automated classification of Persistent Scatterers Interferometry time series. *Natural Hazards Earth System Science*, 13(8), 1945–1958.
- Bouhadad Y., Laouami N. (2002). Earthquake hazard assessment in the Oran region (Northwest Algeria). *Natural hazards*, 26, 227–243.
- C. Colesanti, A. Ferretti, R. Locatelli, F. Novali and G. Savio. (2003). Permanent Scatterers: precision assessment and multi-platform analysis. *IEEE International Geoscience and Remote Sensing Symposium. Proceedings. Toulouse, France*, 2, 1193–1195, DOI: [10.1109/IGARSS.2003.1294055](https://doi.org/10.1109/IGARSS.2003.1294055).

- Colesanti, C., Le Mouélic, S., Bennani, M., Raucoules, D., Carnec, C., Ferretti, A. (2005). Detection of mining related ground instabilities using the permanent scatterers technique - a case study in the east of France. *International Journal of Remote Sensing*, 26(1), 201–207.
- Crossetto, M., Crippa, B., Biescas, E. (2005). Early detection and in-depth analysis of deformation phenomena by Radar interferometry. *Engineering Geology*, 79, 81–91. DOI: <https://doi.org/10.1016/j.enggeo.2004.10.016>.
- Delft Object-oriented Radar Interferometric Software User's manual and technical documentation v4.02. Delft University of Technology, December 2008. <http://enterprise.lrtudelft.nl/doris/>.
- Eineder, M., Holzner, J. (1999). Phase unwrapping of low coherence differential interferograms. *IEEE 1999 International Geoscience and Remote Sensing Symposium. IGARSS'99 (Cat. No.99CH36293)*, Hamburg, Germany, 1999, 3, 1727-1730. DOI: <https://doi.org/10.1109/IGARSS.1999.772076>.
- El Rai, M. C., Simonetto E. (2010). Mesure des déformations du sol par la méthode des réflecteurs permanents StaMPS. *Ecole Supérieure des Géomètres et Topographes ESGT – CNAM*.
- Ferretti, A., Prati, C., Rocca, F. (2001). Permanent Scatterers in SAR interferometry. *IEEE Transactions on Geoscience and Remote Sensing*, 31(1), 8-20.
- Ferretti, A., Fumagalli, A., Novali, F., Prati, C., Rocca, F., Rucci, A. (2011). A new algorithm for processing interferometric data-stacks: SqueeSAR. *IEEE Transactions on Geoscience and Remote Sensing*, 49 (9), 3460–3470. DOI: <https://doi.org/10.1109/TGRS.2011.2124465>.
- Gabriel, A.K., Goldstein, R.M., Zebker, H. A. (1989). Mapping small elevation changes over large areas: Differential radar interferometry. *Journal of Geophysical Research*, 94 (B7), 9183–9191. DOI: <https://doi.org/10.1029/JB094iB07p09183>.
- Hasni, K., Gourine, B., Namaoui, H., Larabi, M. L., Allal, S. H. (2021). Joint Correction of Tropospheric and Orbital Errors in SAR Differential Interferograms. *Anuário do Instituto de Geociências*, 44, 38730. DOI: [https://doi.org/10.11137/1982-3908\\_2021\\_44\\_38730](https://doi.org/10.11137/1982-3908_2021_44_38730).
- Hooper, A., Zebker, H., Segall, P., Kampes, B. (2004). A new method for measuring deformation on volcanoes and other natural terrains using InSAR persistent scatterers. *Geophysical Research Letters*, 31 (23), 1–5. DOI: <https://doi.org/10.1029/2004GL021737>.
- Hooper, A., Segall, P., Zebker H.A. (2007). Persistent scatterer InSAR for crustal deformation analysis, with application to volcán alcedo, Galapagos. *Journal of Geophysical Research*, 112, (B07407).
- Hooper, A. (2008). A multi-temporal InSAR method incorporating both persistent scatterer and small baseline approaches. *Geophysical Research Letters*, 35(16), 1-5.
- Hooper, A., Bekaert, D., Spaans, K., Arikani, M. (2012). Recent advances in SAR interferometry time series analysis for measuring crustal deformation. *Tectonophysics*, 514, 1-13.
- Hooper, A., Bekaert, D., Spaans, K. (2013). *StaMPS/MTI Manual Version 3.3b1*. University of Leeds, <http://homepages.see.leeds.ac.uk/earahoo/stamps/>.
- Hu, L. Y., Li, Y. S., Xing, C. Q., Dai, K.R., Yan, R., Guan, X. (2018). Crustal Deformation Monitoring in Beijing Using Radarsat-2 InSAR Time Series Analysis. In *Proceedings of the International Workshop on Environmental Management, Science and Engineering (IWEMSE 2018)*, 710-717.
- Konakoğlu, B. (2020). Analysis of dam deformation with robust weight functions. *Geodetski-Vestnik*, 64 (2), 198-213. DOI: [10.15292/geodetski-vestnik.2020.02.198-213](https://doi.org/10.15292/geodetski-vestnik.2020.02.198-213).
- Biswas, K., Chakravarty, D., Mitra, P., Arundhati, M. (2017). Spatial-correlation based persistent scatterer interferometric study for ground deformation. *Journal of the Indian Society of Remote Sensing*, 45, 913–926. DOI: <https://doi.org/10.1007/s12524-016-0647-5>
- Liu, Y., Lu, Z., Zhao, C., Kim, J., Zhang, Q., Fuente, J. (2019). Characterization of the kinematics of three bears landslide in northern California using L-band InSAR observations. *Remote Sensing*, 11, 2726, DOI: [10.3390/rs11232726](https://doi.org/10.3390/rs11232726).
- Lundgren, P., Usai, S., Sansosti, E., Lanari, R., Tesauro, M., Fornaro, G., Berardino, P. (2001). Modeling surface deformation observed with synthetic aperture radar interferometry at Campi Flegrei caldera. *Journal of Geophysical Research*, 106(19), 355-366.
- Mammar, L., Mouli, M., Senouci, A., Said, A., Allout, A. (2016). Indices de vulnérabilité des constructions existantes à oran (indices of vulnerability of existing buildings in oran). *Journal of Materials and Environmental Sciences*, 7(3), 942-955.
- Massonnet, D., Feigl, K. (1998). Radar interferometry and its application to changes in the earth's surface. *Reviews of Geophysics*. 36 (4), 441–500. DOI: <https://doi.org/10.1029/97RG03139>.
- Massonnet, D., Souyris, J. C. (2008). *Imaging with synthetic aperture radar*. EPFL press.
- Perissin, D., Wang, T. (2012). Repeat-pass SAR interferometry with partially coherent targets. *IEEE Transactions on Geoscience and Remote Sensing*. 50 (1), 271–280. DOI: <https://doi.org/10.1109/TGRS.2011.2160644>.
- Qiu J., Liu L., Wang C., Wang Y. (2019). Present-day tectonic activity along the central section of the Altyn Tagh fault derived from time series InSAR. *Geodesy and Geodynamics*, 10(4), 307-314. DOI: <https://doi.org/10.1016/j.geog.2019.03.008>.
- Roukh, Z. A. (2021). *Cartographie algébrique d'aléa multirisque du Littoral Oranais*, PhD thesis, Oran University Algeria, NO de l'Algérie Risques .
- Solaro, G., Acoella, V., Pepe, S., Ruch, J., Neri, M., Sansosti, E. (2010). Anatomy of an unstable volcano from InSAR: Multiple processes affecting flank instability at Mt. Etna, 1994–2008. *Journal of Geophysical Research*, 115(B10405). DOI: [10.1029/2009JB000820](https://doi.org/10.1029/2009JB000820).
- Yan, L., Li, Z., Li, Z., & Zhang, L. (2018). Comparison of PS-InSAR and SBAS for land subsidence monitoring in Beijing based on Sentinel-1A data. *Remote Sensing*, 10(10), 1662.
- Zebker, H. A., Villasenor, J. (1992). Decorrelation in interferometric radar echoes. *IEEE Transactions on Geoscience and Remote Sensing*, 30(5), 950-959.

Zhao, Q., Ma, G., Wang, Q., Yang, T., Liu, M., Gao, W., Falabella, F., Mastro, P., Pepe, A. (2019). Generation of long-term InSAR ground displacement time-series through a novel multi-sensor data merging technique: The case study of the Shanghai coastal area. *ISPRS Journal of Photogrammetry and Remote Sensing*, 154, 10-27. DOI: <https://doi.org/10.1016/j.isprsjprs.2019.05.005>.

Zhang, Z., Hu, C., Wu, Z., Zhang, Z., Yang, S., Yang, W. (2023). Monitoring and analysis of ground subsidence in Shanghai based on PS-InSAR and SBAS-InSAR technologies. *Scitific Repports*, 13. DOI: <https://doi.org/10.1038/s41598-023-35152-1>.



Hasni K., Gourine B., Boubaker B., El Amine S. M. (2024). Assessing Ground Displacement in Oran City, Algeria: A Comparative Analysis of PSInSAR, SBAS, and Combined Method. *Geodetski vestnik*, 68 (4), 432-450.  
DOI: <https://doi.org/10.15292/geodetski-vestnik.2024.04.432-450>

**Kamel Hasni Ph.D.**

*Space Geodesy Department, Centre of Space Techniques (CTS),  
Arzew, Algeria.  
01, Avenue de la Palestine, BP. 13, Arzew, 31200, Algeria  
e-mail : hasni.kamel@gmail.com*

**Boudhane Boubaker, Ph.D. candidate**

*Space Geodesy Department, Centre of Space Techniques (CTS),  
Arzew, Algeria.  
01, Avenue de la Palestine, BP. 13, Arzew, 31200, Algeria  
e-mail : boudhaneboubaker@gmail.com*

**Bachir Gourine, Ph.D.**

*National Higer School of Geodetic Sciences and  
Space Techniques (ENSGTS)  
01, Avenue de la Palestine, BP. 14, Arzew, 31200, Algeria  
e-mail : bachourgourine@yahoo.com*

**Slimani Mohammed El Amine, Ph.D. candidate**

*Space Geodesy Department, Centre of Space Techniques (CTS),  
Arzew, Algeria.  
01, Avenue de la Palestine, BP. 13, Arzew, 31200, Algeria  
e-mail : sssmedamine@gmail.com*